

Chapter Title: Detectors and Measurements

Book Title: Elementary Particle Physics in a Nutshell

Book Author(s): Christopher G. Tully

Published by: Princeton University Press. (2011)

Stable URL: <https://www.jstor.org/stable/j.ctvcmxp3f.8>

JSTOR is a not-for-profit service that helps scholars, researchers, and students discover, use, and build upon a wide range of content in a trusted digital archive. We use information technology and tools to increase productivity and facilitate new forms of scholarship. For more information about JSTOR, please contact support@jstor.org.

Your use of the JSTOR archive indicates your acceptance of the Terms & Conditions of Use, available at <https://about.jstor.org/terms>



Princeton University Press is collaborating with JSTOR to digitize, preserve and extend access to *Elementary Particle Physics in a Nutshell*

Contrary to how we have discussed elementary particle physics up to this point, the basic experimental observables in a detector are not four-vectors. It is also rare for one single type of detector to provide enough information to identify the particles coming from a high-energy interaction and measure their energies and momenta. High-energy experiments are, therefore, collections of detectors that each provide some level of particle identification (PID) and kinematic measurement. To get a global view of what particles have been produced subsequent to a given high-energy interaction requires piecing together the information from a half dozen different detector subsystems. Rather than go over different types of detectors and their use as a starting point, the discussion below is organized from the perspective of the type of particle or object to be measured, followed by a review of the different experimental handles that exist for these measurements. Discussions of major detector topics are invoked as needed to explain the experimental methods that are involved.

5.1 Photons and Electromagnetic Calorimeters

Photons are primarily detected by their interaction with an *electromagnetic calorimeter*. To understand the function of a calorimeter, treat each particle incident on a volume of matter as a fixed-target experiment. The behavior of a particle interacting with the material will be governed by the largest cross-section processes. For electromagnetically interacting particles, the largest cross sections occur at low-momentum transfer ($1/q^2$ in the photon propagator) in regions of the material where there is a strong Coulomb source from nonzero net nuclear charge:

$$\frac{1}{r_{\text{atom}}} < |q| < \frac{1}{r_{\text{nucleus}}}. \quad (5.1)$$

A two-vertex electromagnetic interaction at low transverse momentum has a cross section set by the classical electron radius, $r_e = \alpha_{\text{QED}}/m_e$, in the Thomson formula $8\pi r_e^2/3 \approx 0.665$

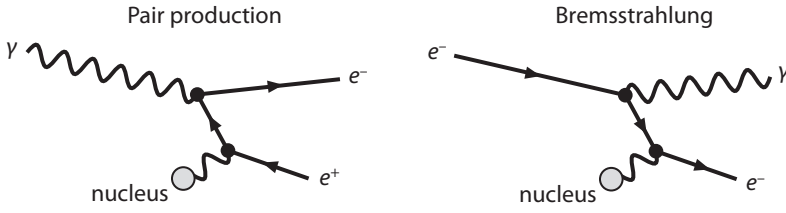


FIGURE 5.1. On the left, pair production of an electron-positron pair from a photon interacting with the charge of a nucleus. On the right, Bremsstrahlung, or “braking,” radiation of a photon off of an electron or positron interacting with the charge of a nucleus.

barn. A radiative process, i.e., one with an extra photon external leg or external Coulomb source, will have an additional power of α_{QED}/π and a photon propagator integral over the length scales where there is a Coulomb source from unscreened nonzero nuclear charge in the volume of the material, as shown in figure 5.1.

The electron-positron pair production cross section, as for *Bremsstrahlung*, meaning “braking radiation,” can be approximated by applying one power of α_{QED} per interaction vertex and a photon propagator momentum integral over the appropriate inverse length scales

$$\sigma_{\text{radiative}} \approx \pi r_e^2 \left[\left(\frac{Z^2 \alpha}{\pi} \right) \int_{1/r_{\text{atom}}^2}^{1/r_{\text{nucleus}}^2} \frac{dq^2}{q^2} \right] = 2\alpha \left(\frac{\alpha}{m_e} \right)^2 Z^2 \ln \left(\frac{r_{\text{atom}}}{r_{\text{nucleus}}} \right) \quad (5.2)$$

where the pair production cross section is a factor of 7/9 smaller than that for *Bremsstrahlung* due to differing terms in the invariant amplitude. For a material with N atoms per cm^3 , there will be on average n collisions in a path length L related by

$$n = N \sigma_{\text{radiative}} L. \quad (5.3)$$

Setting $n = 1$ and writing $L = X_0$, the inverse *radiation length*, X_0^{-1} , is given by

$$\frac{1}{X_0} = N \sigma_{\text{radiative}} \approx 4N\alpha \left(\frac{\alpha}{m_e} \right)^2 Z^2 \ln \left(\frac{183}{Z^{1/3}} \right), \quad (5.4)$$

where the additional factor of 2 comes from the inverse dependence of the atomic and nuclear radii on the nuclear charge in the logarithm, i.e., $r_{\text{atom}} \propto Z^{-1/3}$ while $r_{\text{nucleus}} \propto Z^{1/3}$. The factor of 183 in the logarithm is a numerical approximation for the square root of the ratio of atomic and nuclear length scales. Therefore, for energetic photons, well above the mass threshold for pair production, the interaction with matter takes on the form of an *electromagnetic cascade* or *shower*, whereby at a characteristic distance of X_0 in a material, all photons in the shower pair produce and all electrons and positrons undergo *Bremsstrahlung*. Thus, the average energy of a particle in the shower drops to $E_0/2^n$, corresponding to the total multiplicity of particles in the electromagnetic shower at that depth, where E_0 is the incident photon energy and n is the number of X_0 into the shower. Once the energy drops down to on order 10 MeV, a growing fraction of $1 \rightarrow 1$ processes occur, such as *Compton scattering*, *photoelectric interactions*, and *ionization*. Only about 25% of the total energy

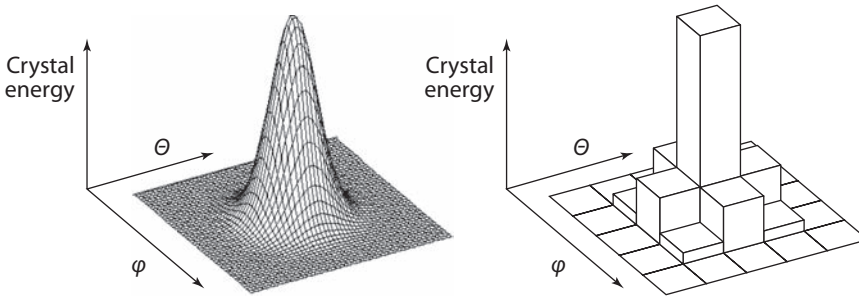


FIGURE 5.2. Transverse shower shape of a photon in an electromagnetic calorimeter composed of inorganic scintillating crystals, shown on the left. The two axes are the cylindrical coordinates of a barrel geometry calorimeter. The right-hand side shows the typical granularity of a detector where the cell size is comparable to the Molière radius of the shower in the material. Typically nine crystals contain 99% of the lateral shower energy.

deposited by the shower in the material is from positron interactions. There are two orders of magnitude more liberated atomic electrons in the shower than positrons. The large multiplicity of particles in the shower allows one to use the transverse and longitudinal shape of the shower to identify the incident particle as electromagnetic, i.e., an electron, positron, or photon. Figure 5.2 shows the transverse shower profile of a photon and a typical transverse segmentation of an actual detector, where the segmentation is set comparable to a characteristic transverse size known as the Molière radius. The thickness of the electromagnetic calorimeter is typically 20–25 radiation lengths, ~ 25 cm for high-density crystal calorimeters, in order to keep the longitudinal containment fluctuations below $\sim 0.5\%$.

For a calorimeter based on scintillating crystals, the statistics of the light yield and photodetection factor into the stochastic term S in the energy measurement. An equivalent term arises in ionization-based cryogenic liquid calorimeters where the linear dimension, d_{active} [mm] of the liquid gap, typically 2–3 mm, and the *sampling fraction* f_{samp} , typically 1–2%, of the energy loss in the liquid compared to the passive absorbers give a stochastic term $S \approx 2.7\% \sqrt{d_{\text{active}}[\text{mm}]/f_{\text{samp}}}$. Other contributions to the energy resolution, added in quadrature, are from electronic noise N and a percentage error on the energy measurement, known in the fractional energy resolution as a *constant term* C . The fractional energy resolution is parameterized by

$$\frac{\sigma_E}{E} = \frac{N}{E} \oplus \frac{S}{\sqrt{E}} \oplus C, \quad (5.5)$$

where σ_E is the Gaussian standard deviation of the energy measurement relative to the mean response with E in units of GeV. The symbol \oplus means addition in *quadrature*:

$$\frac{N}{E} \oplus \frac{S}{\sqrt{E}} \oplus C \equiv \sqrt{\left(\frac{N}{E}\right)^2 + \frac{S^2}{E} + C^2}. \quad (5.6)$$

Ultimately, the constant term is the limiting factor on the resolution of high-energy measurements. The constant term comes from intrinsic nonuniformities in the calorimeter

response, including from cell-to-cell energy calibration inaccuracies. An electromagnetic calorimeter will typically have a stochastic term varying from $S = 3\text{--}15\%$, with $\sim 3\text{--}5\%$ typical for crystal calorimeters and $\sim 10\text{--}15\%$ typical for sampling calorimeters, and a constant term $C = 0.5\text{--}2\%$ with an electronic noise in the range $N = 0.1\text{--}0.5$ GeV.

5.2 Electrons, Tracking, dE/dx , and Transition Radiation Detectors

An electron is distinguished from a photon primarily by the presence of a *charged track* pointing directly at the center of the electromagnetic shower. A *charged track* is a term used for a measurement of the trajectory of a charged particle using detectors known as trackers.

When a charged particle passes in proximity to an atomic electron, there is a finite probability that the atomic electron is excited into the conduction band of the material. In a gaseous medium, the atomic electron is liberated in this process, thereby leaving an ionized molecule, or ion. If an ambient electric field is applied across the tracker medium, then the ionized charges in a gas, or electron-hole pairs in a semiconductor, will separate. Under normal material densities and electric field strengths, the electrons due to a finite mean-free path length will drift at a constant velocity, known as the *drift velocity*, and similarly for the ions, but at a substantially lower velocity. The charge is drifted to anodes and cathodes and collected. If the drift velocity is sufficiently low, then the drift time, the time that elapses before the charge is incident on the collection electrode, is used as a means to compute the spatial coordinate of where the initial ionization occurred within the tracking volume. In a silicon strip tracker, a thin, typically $300\text{ }\mu\text{m}$ thick silicon wafer with metallization for charge collection at a fine spacing, such as $50\text{ }\mu\text{m}$, will detect ionization charge across several closely spaced strips forming a *charge cluster*. Correcting for possible shifts from an effect known as the *Lorentz angle* due to drift in ambient electric and magnetic fields, the center of the charge cluster is a spatial measurement of the location where the charged particle passed through the silicon detector.

A tracker is, therefore, a device that measures spatial coordinates along the trajectory of a charged particle. The spatial measurement is made directly with charge clusters or indirectly with drift time measurements. The spatial coordinates along a charged particle trajectory need to be associated with the same track in order to accurately measure the properties of the trajectory, such as the proximity of the track to the collision point, the impact point of the track on the calorimeter, and any bending or curvature that the track has due to motion in an ambient magnetic field. A tracker, unlike a calorimeter, competes with the necessity to make measurements without interfering with the properties of the charged particle.

An ideal helicoidal track requires five parameters, where one choice of parameters in the bending plane is the curvature, the azimuthal angle of the momentum at the position of closest approach to a reference point and the distance of closest approach to the reference point. For a circular trajectory in the bending plane, the transverse momentum p_T (in GeV/ c) is related to the radius of curvature R (in m) in a magnetic field B (in T) via

$$p_T = 0.2998BR \quad (5.7)$$

where the significant digits come from the speed of light $c = 2.99793 \times 10^8$ m/s. The *sagitta* $s \approx 0.3BL^2/(8p_T)$ is the maximum deviation of the track from a straight line, which for a tracker lever arm, or chord, $L = 1$ m, a magnetic field $B = 4$ T, and $p_T = 1000$ GeV/c gives a sagitta of $150 \mu\text{m}$. In the nonbending plane for an arbitrary helicoidal trajectory, an offset and slope are typical parameters.

The most important degrading effect from material on the performance of the tracking system is called *multiple scattering*. If a charged particle bending in a magnetic field passes through a length of tracker material, then it will be randomly deflected with a characteristic opening angle depending on the density and thickness of the material. Fortunately, the larger the magnetic field, the smaller the percentage deflection of the charged particle relative to the deflection expected from the motion in the field. Therefore, multiple scattering is reduced for high magnetic fields down to a typical level of 0.5–2% of the track momentum transverse to the direction of the magnetic field. This momentum resolution limit is flat over a finite range of track momenta. Below typically 50–100 MeV/c in p_T , the track curls in the magnetic field and eventually stops in the material. For large transverse momenta, the track will have little deflection in the magnetic field and the finite curvature cannot be distinguished from a straight trajectory, leading to the possibility of a mismeasurement of the sign of the curvature, known as *charge confusion*. One can parameterize the transverse momentum resolution of a tracker as

$$\frac{\sigma_{p_T}}{p_T} = c_0 \oplus c_1 \cdot p_T \quad (5.8)$$

added in quadrature according to equation (5.6) where σ_{p_T} is the Gaussian standard deviation, or uncertainty, of the measurement relative to the mean p_T , the component of the momentum orthogonal to the ambient magnetic field. The multiple-scattering term dominates for most of the low- p_T momentum range with a constant percentage error $c_0 = 0.5\text{--}2\%$. The second term is a limitation of the momentum resolution from the measurement of the finite curvature of the track where for a value of $c_1 = 10^{-3}\text{--}10^{-4} (\text{GeV}/c)^{-1}$ will begin to dominate for p_T greater than 100 GeV/c. Typically, LHC experiments design their tracking systems to maintain 10% momentum resolution or better at a momentum of 1 TeV/c. The term c_0 grows as the square root of the thickness of the tracker in units of radiation length, but depends on the inverse of the magnetic field strength and therefore leads to high-field magnets to compensate for tracker material. The term c_1 is inversely proportional to BL^2/σ_{hit} , where L is the tracker radius or “lever arm” of the curvature measurement and is typically $L = 1\text{--}2$ m. The single hit resolution σ_{hit} for a silicon tracker can be as low as $10\text{--}50 \mu\text{m}$, or even smaller for the centroid of a charge cluster, while a gas drift chamber is typically $100\text{--}150 \mu\text{m}$. For electron measurements, it is useful to know when the momentum resolution of the tracker, which is given by the multiple-scattering term at low p_T , is superseded by the energy measurement resolution of the electromagnetic calorimeter. It’s not uncommon for two measurement resolutions to be equal in the vicinity of 30–40 GeV depending on the detector parameters. Typically, the tracker elements are first aligned with straight, zero-ambient magnetic-field charged tracks. Then,

the tracker is used to cross-calibrate the calorimeter up to the energy scale where the resolutions are comparable.

When the integrated tracker thickness is comparable to a radiation length, then electrons will undergo the Bremsstrahlung process within the tracker volume and liberate photons along its trajectory. Similarly, photons will have a finite probability to “convert” into closely spaced electron-positron tracks through the pair-production process. Therefore, for the measurement of electron trajectories there is a competing trade-off between increasing the number of spatial measurements along the trajectory and reducing the probability for radiative processes that degrade the ability to match the charged track to a well-shaped electromagnetic shower in the calorimeter. Tracker-based methods for identifying electrons in advance of the electromagnetic calorimeter are therefore also important. One method relies on measuring the magnitude of the ionization by a charged particle in the tracker layers, a technique known as dE/dx . The magnitude of dE/dx for muons is given by the Bethe-Bloch formula [1] plotted in figure 5.3. The rate of dE/dx energy loss has a shallow minimum starting at $\beta\gamma \approx 1$ extending to $\beta\gamma = 100\text{--}1000$. The lowest value of dE/dx is at $\beta\gamma = 3\text{--}3.5$, known as *minimum ionizing*, with a typical value of $(1.5/\rho)$ MeV cm²/g normalized to the density of the material. Copper, for example, has a density of $\rho = 9$ g/cm³ giving $dE/dx = 13.5$ MeV/cm. Most long-lived charged particles produced in collider experiments, typically at momenta of a few to tens of GeV/c, such as muons, pions, and kaons, are *minimum ionizing particles (MIPs)* over a wide range of momentum as set by $\beta\gamma$. However, the electron, which has additional scattering processes with atomic electrons and significant radiative losses due to its small mass, is typically $1.3\text{--}1.6 \times$ minimum ionizing over the same range of momenta. The dE/dx measurement in combination with the momentum measurement can therefore be used for particle

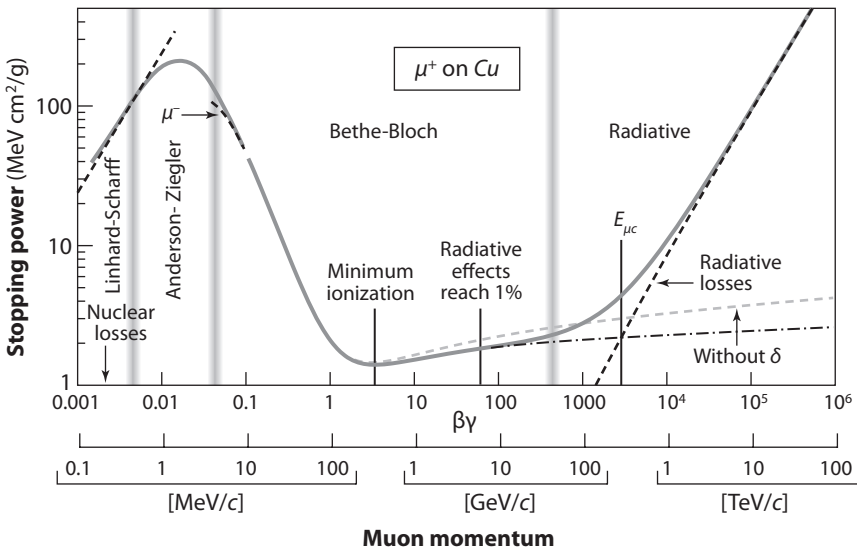


FIGURE 5.3. Rate of energy loss for a μ^+ traveling through copper normalized to the density of copper (Credit: PDG) [1].

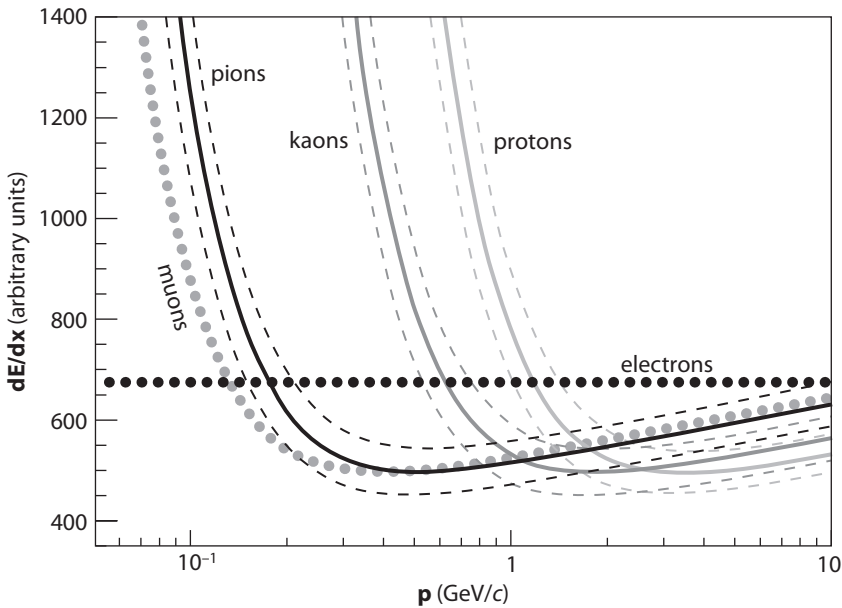


FIGURE 5.4. The measurement of dE/dx for different particle types as a function of momentum (Credit: BABAR). The dashed bands indicate the typical measurement resolutions.

identification at low momentum, as shown in figure 5.4. A second class of particle identification methods relies on the large Lorentz boost of the electron in the lab frame. An effect discovered in 1939, known as *transition radiation* [1, 2], causes relativistic electrons to emit X-rays as they pass from a dielectric into a gas-filled vacuum. The flux of emitted X-rays when absorbed by a high-Z gas layer effectively results in the enhancement of the dE/dx signal from electrons, thereby improving the electron identification.

5.3 Single Hadrons, Time-of-Flight, Cherenkov Radiation, and Hadron Calorimeters

The total interaction cross section of a hadron is an order of magnitude smaller, roughly 40 mb, than for an *electromagnetic particle*, i.e., an electron, positron, or photon, interacting with the same calorimeter material. The large spatial extent of hadronic showers forces hadronic calorimeters to be thick, massive detectors, using dense materials such as copper, iron, lead, uranium, and tungsten to provide shower containment. The particular choice of absorber material can depend on the mechanical strength requirement, such as the need to maintain a precise gap spacing (i.e., no sagging) over a large distance, the need for nonmagnetic materials, or the use of self-calibrating fission signals. Unlike an electromagnetic shower, the particle multiplicity per interaction in a hadronic shower is not constant. The first interaction will have the highest particle multiplicity, on order 10 secondary particles for an incident pion of 300 GeV, with the multiplicity growing

logarithmically with incident pion energy. The second set of interactions will drop down, for the given example, to the level of 6 secondary particles per interaction on average, and the third set to $1 \rightarrow 3$ processes. By the fourth interaction length, $1 \rightarrow 1$ processes begin to dominate and the number of showering particles begins to drop off. The average shape of a hadron shower thus has a much sharper rise of energy deposition in the first nuclear interaction length than an electromagnetic shower. And, unlike a radiation length, the nuclear interaction length is less universal. Typically one refers to the proton nuclear interaction length when describing calorimeters, while, in fact, the pion nuclear interaction length is 1.5 times longer and can lead to a small probability for charged pions to fully penetrate the hadron calorimeter, an occurrence known as *punch-through*. Typically and for practical reasons, hadron calorimeters are limited to ~ 10 (proton) nuclear interaction lengths in thickness, i.e., 1.1–1.7 m.

Hadronic showers are challenging to measure due to the irregularity of their shape and fluctuations in particle content and multiplicity. A large number of neutrons are liberated in the shower from nuclear break-up and only a fraction of the neutron energy is collected within the integration time of the calorimeter energy measurement. There are fluctuations in the particle multiplicity per interaction, and an important effect comes from the asymmetry in charged pion and neutral pion energy depositions. Nuclear interactions will allow nuclear isospin quantities to “tumble” freely in the shower. However, if a charged pion tumbles into a π^0 or a π^0 is produced, the π^0 decays promptly via $\pi^0 \rightarrow \gamma\gamma$ and, therefore, immediately initiates an electromagnetic shower. Thus, for every nuclear interaction length into the hadron calorimeter, there is a finite probability for an electromagnetic shower to occur within the hadronic shower. The π^0 fraction f_{π^0} , the so-called electromagnetic component of hadronic showers, grows nonlinearly with incident hadron energy and imparts a nonlinear energy response in calorimeters due to unequal efficiencies for measuring electromagnetic (e) shower energies as compared to hadronic (h) energy depositions and ionization, known as the e/h -value. A calorimeter with $h/e = 1$ is known as *compensating*. Noncompensating calorimeters typically have larger stochastic and constant terms than the ideal, compensating calorimeters. In fact, out of geometric necessity, the electromagnetic calorimeter typically acts as the first interaction length of the hadron calorimeter measurement and this can further contribute to a nonuniform response if the EM calorimeter has a different e/h -value or there are significant amounts of dead material between the EM and hadronic compartments. One nuclear interaction length will typically not be sufficient to contain a hadronic shower (exceptions are early electromagnetic showering from *charge-exchange processes* where a charge pion converts directly to a π^0). Therefore, hadrons can be separated from electrons by requiring some fraction of the total calorimeter energy to be deposited in the hadronic calorimeter, the so-called H/E -ratio of hadronic to electromagnetic calorimeter energy. The energy measurement resolution of a hadron calorimeter can be expressed in the same form as electromagnetic calorimeters (5.5). However, in contrast to an EM calorimeter, the parameters for a hadron calorimeter are typically an order of magnitude larger with the stochastic term in the range $S = 45\text{--}125\%$, the constant term $C = 4\text{--}8\%$, and the noise term 1–5 GeV.

Particle identification for hadrons can be achieved with detectors that sit in front of the calorimeters and make measurements related to the finite velocity of the hadron. In recent years, the level of precision of spatial measurements, now down to the sub-10 μm level, has been complemented with time-of-flight systems that can achieve sub-10 ps timing resolution. These systems use thin devices with low transit-time readout electronics, such as fast radiators coupled to silicon photomultiplier detectors or chambers that look for ionization-induced discharges across a thin high-voltage gap. Two different hadrons originating at the same vertex with the same momentum p , such as a charged pion and a charged kaon, will have a time-of-flight difference at a distance L from a common vertex given by

$$\Delta t \approx \frac{Lc}{2p^2} (m_K^2 - m_\pi^2), \quad (5.9)$$

which shows that for flight distances of $L = 1$ m, a high-precision time-of-flight detector separates kaons from pions for momenta up to a few GeV/c .

The fast radiator is a substance such as quartz with a high index of refraction. A form of radiation known as *Cherenkov radiation* is emitted when a particle travels in a medium at a velocity that exceeds the maximum propagation velocity of electromagnetic radiation within that material. The flux of Cherenkov light, whose frequency spectrum starts in the blue and goes into the ultraviolet, has a conical opening angle that depends on the quantity

$$\cos \theta_c = \frac{1}{\beta n(\lambda)} \quad (5.10)$$

where $\beta = v/c$ is the velocity of the particle normalized to the speed of light in vacuum and $n(\lambda)$ the wavelength-dependent index of refraction of the medium. The opening angle of the radiation, θ_c , is used for a type of particle identification system known as a Ring-Imaging CHerenkov (RICH) detector, where the rings correspond to the time expansion of the Cherenkov radiation and subsequent measurement with a dense spatial array of UV-sensitive photodetectors. In its most compact form, ring-imaging information can be preserved and transported using a highly polished quartz panel exhibiting internally reflected Cherenkov light. The momentum-dependent particle identification system using the Detection of Internally Reflected Cherenkov (DIRC) radiation is shown in figure 5.5.

Hadrons that decay promptly or within the tracker volume can be identified using resonance reconstruction, as in the case of $K_S^0 \rightarrow \pi^+ \pi^-$ and $\pi^0 \rightarrow \gamma \gamma$ shown in figures 5.6 and 5.7, respectively.

5.4 Muons and Muon Spectrometers

The muon is unique in that it is the only long-lived charged particle with minimal cross section to interact with matter for momenta up to nearly 1 TeV/c . A muon will therefore pass through the central tracker, the electromagnetic and hadronic calorimeters, and the

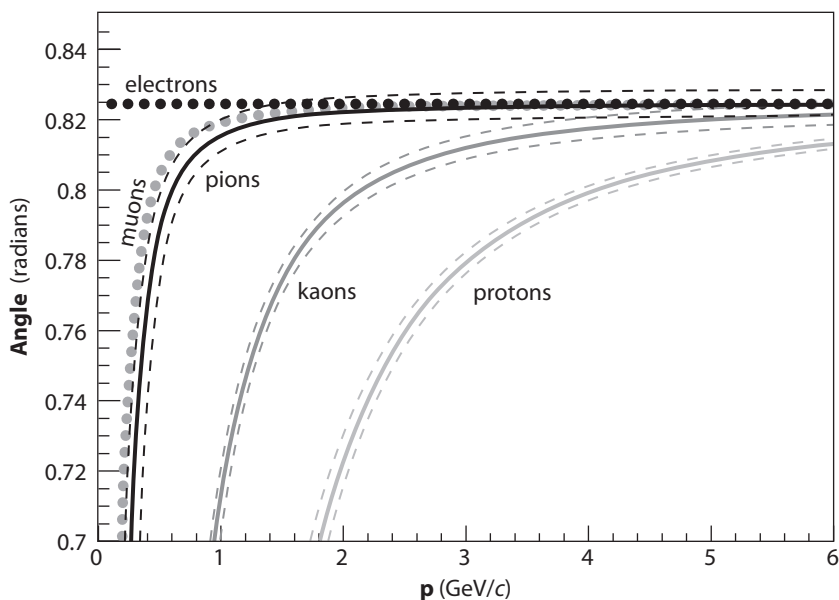


FIGURE 5.5. The opening angle of Cherenkov radiation emitted from different particle types as a function of momentum (Credit: BABAR). The Cherenkov light is internally reflected in a DIRC detector before being measured. The dashed bands indicate the typical measurement resolutions.

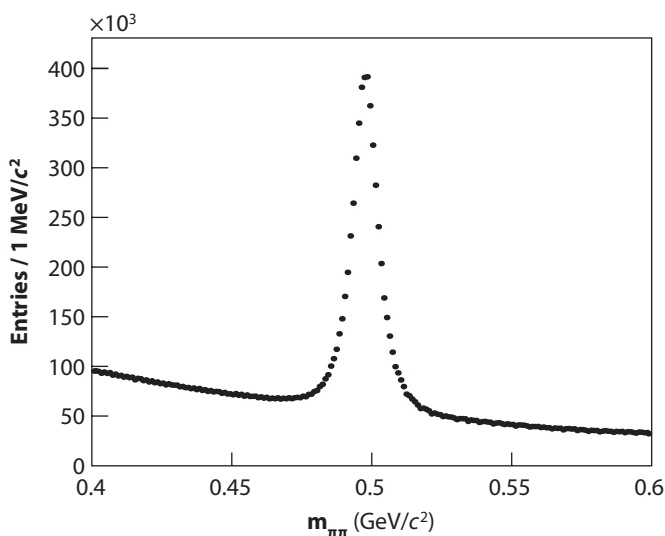


FIGURE 5.6. Invariant mass distribution of a $\pi^+ \pi^-$ secondary vertex showing a resonance peak at the K_S^0 mass in $\sqrt{s} = 7$ TeV data collected by the CMS experiment (Credit: CMS) [3].

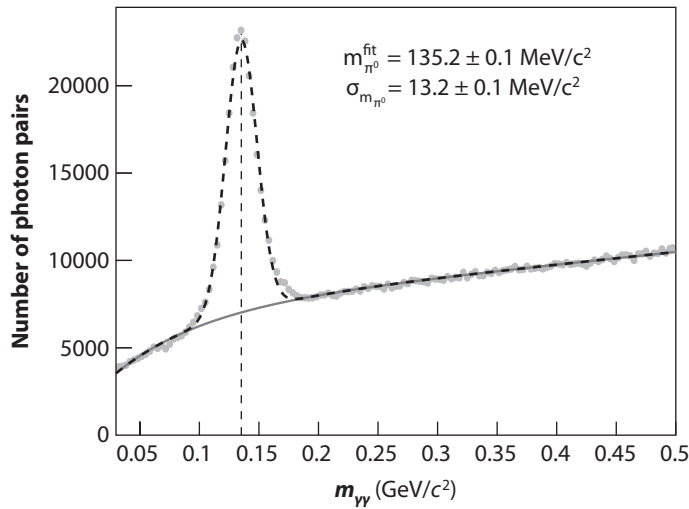


FIGURE 5.7. The diphoton reconstructed invariant mass from π^0 decays collected by the CMS experiment using $\sqrt{s} = 7$ TeV data (Credit: CMS) [3]. The baseline under the peak comes mainly from the combinatorial background of diphoton selection.

magnet coil with only *minimum ionizing* energy loss, typically losing 2–3 GeV of total energy in the calorimeters. An example trajectory of a muon in the CMS experiment and a summary of several of the particle measurement techniques is shown in figure 5.8 for a slice of the many detector subsystems comprising the experiment. The bending of the muon reverses sign outside of the solenoid due to the return flux of the magnetic field concentrated within the layers of iron interspersed between tracking chambers, known as the *muon spectrometer* or instrumented return flux. The additional lever arm of the muon spectrometer complements the combined tracking momentum resolution by reducing the effective c_1 term in equation (5.8) relative to using only the inner tracker and thereby improving momentum measurements for charged particles of several hundred GeV/ c to beyond 1 TeV/ c . At low momenta, the multiple scattering term, c_0 , is substantially larger for the stand-alone muon spectrometer and, consequently, the primary function of the muon chambers is to identify the muon as a minimum ionizing charged particle escaping the calorimeters. The calorimeters are typically at least 10 nuclear interaction lengths thick to suppress the probability that a charged hadron can *punch through* and leave a track in the muon chambers.

5.5 Jets and Jet Algorithms

Quarks and gluons that are produced from an elementary interaction will propagate for on order 10^{-23} s before the energy uncertainty of the strongly interacting system begins to

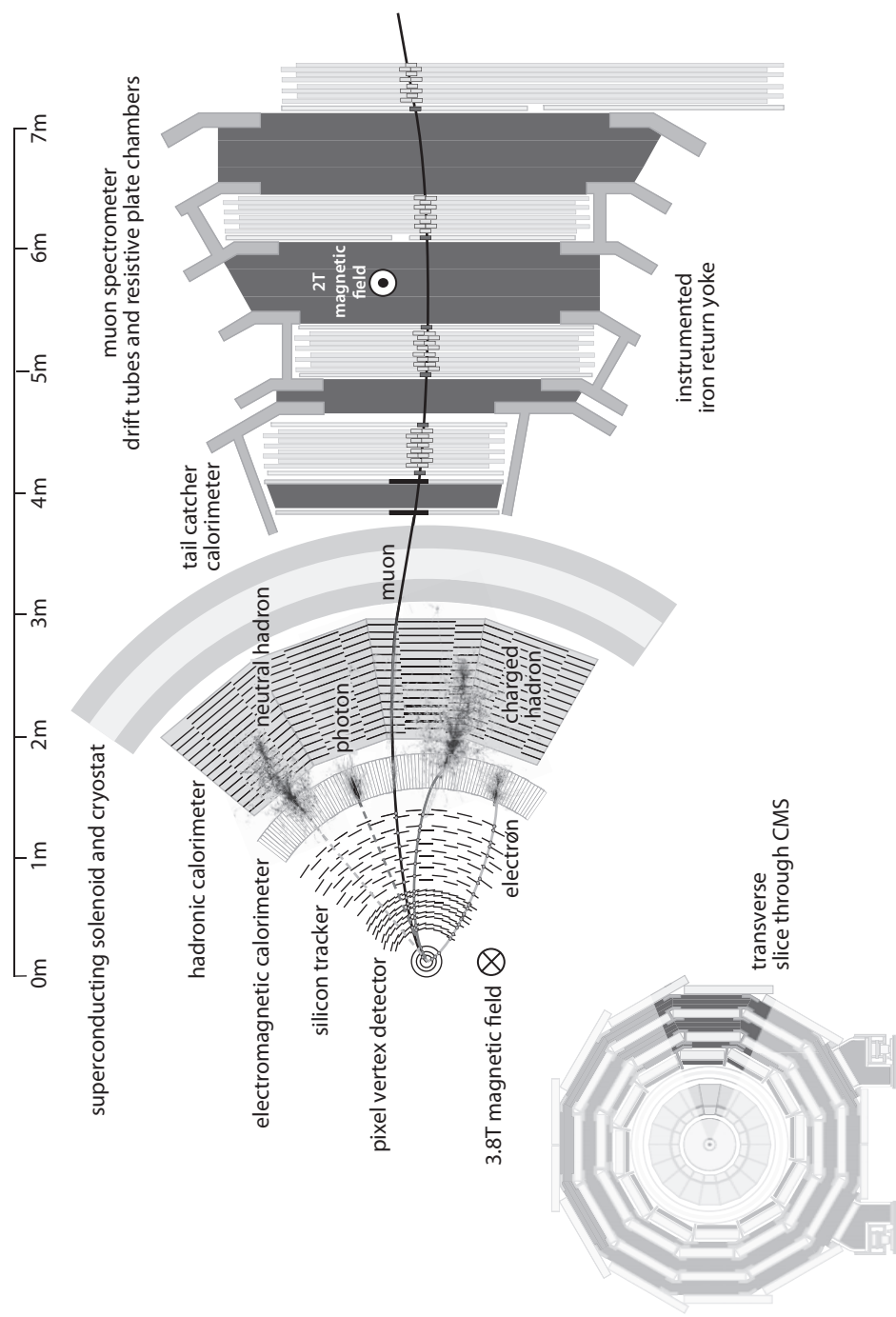


FIGURE 5.8. A schematic view of a slice of the CMS experiment and the corresponding interactions of muons, electrons, photons, and charged and neutral hadrons in elements of the detector (Credit: CMS/D. Barney) [3].

be comparable to the natural widths of color-neutral hadronic bound states that can be directly formed from quark-antiquark pair production in the color potential. Within this time scale, the initial quark or gluon transfers its energy and momentum into a collection of hadrons, some of which promptly decay to other hadrons while others will propagate for much longer time scales. Long-lived hadrons are those that decay through the weak or electromagnetic interactions, or are stable, as in the case of the proton and antiproton. The phenomenon of hadron production initiated by a strongly interacting quark or gluon is known as *QCD jet production*. The bulk of the particles in jets are pions, with an equal number (nuclear isospin independent) on average of π^+ , π^- and promptly decaying $\pi^0 \rightarrow \gamma\gamma$. The heavier mesons and vector mesons are produced at an order of magnitude smaller fractions, on average. Typically, only 10% of the particles produced are baryons and antibaryons. As the overall energy and momentum of the collection of hadrons is set by the initial strongly interacting particle, known as a *parton*, the jet properties are an indirect measure of the initial parton four-momentum. Moreover, the *virtuality* of the initial parton and the effects of λ_{QCD} -scale interactions contribute to a finite jet mass, as computed from the four-momenta of the jet of hadrons. One particular parton, however, the top quark will not directly initiate a QCD jet. Top quark physics will be discussed separately in a later chapter. The weak charged-current decay of the top quark is on a shorter time scale than the strong interaction and, therefore, the top quark does not hadronize before decaying to a *b*-quark and a W boson.

The kinematical quantities corresponding to a QCD jet involve three distinct levels of development. QCD matrix elements assign a four-momentum to the initial parton forming the jet and associated *parton showering* processes such as gluon radiation and quark-antiquark pair production above a perturbative momentum scale k_T . The *perturbative QCD* stage of jet development creates a shower of partons, known as parton-level jets. After the jet momentum sharing among particles in the low- p_T development of the jet, known as *fragmentation*, and the associated *hadronization* into color-neutral hadrons has occurred, the jet is referred to as a particle-level jet. The particle-level jet consists of all stable particles, optionally excluding prompt noninteracting particles such as neutrinos from semi-leptonic heavy quark decay, and corresponds to what an ideal calorimeter (and muon system) is expected to measure. Detector-level jets formed from a combination of calorimeter and tracking measurements for charged particles, as in *particle-flow* techniques, are treated similarly. The calorimeter-level or detector-level jet is composed of the measured energy depositions from the electromagnetic and hadronic showering in the calorimeter and muons measured with tracking detectors and muon spectrometers. These stages of jet development are shown in figure 5.9. Many factors, measurement-related and algorithmic, introduce nonideal jet energy response. The jet energy scale corrections and scale uncertainties for measured jets are typically factorized into calorimeter-to-particle level and particle-to-parton level. The particle-to-parton-level correction depends on the hypothesis for the parton-type initiating the jet and includes energy radiated out of the cone of the reconstructed jet. The jet energy scale corrections depend on every step of jet reconstruction from thresholds in the calorimeter, to jet algorithm and seed thresholds, to detector response and shower containment, to parton-type hypothesis.

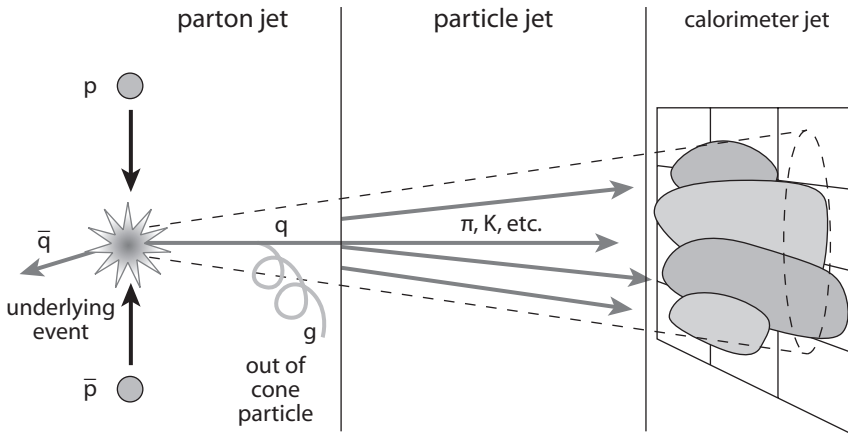


FIGURE 5.9. The three levels of jet development corresponding to QCD matrix element (parton-level), fragmented and hadronized stable particles (particle-level) and detector measurements (calorimeter-jets) (Credit: CDF).

The first jet algorithms for hadron physics, proton-proton and proton-antiproton colliders, were simple cones with a cone radius defined in coordinates that are invariant under Lorentz boosts along the momentum direction of the incoming proton. The *rapidity* y is given by

$$y = \frac{1}{2} \ln \left(\frac{E + p_z}{E - p_z} \right) \quad (5.11)$$

and is explicitly invariant under longitudinal boosts as will be described later in the section on hadron collider physics. In the limit of massless particles

$$E \pm p_z = E(1 \pm p_z/E) = E(1 \pm \beta \cos \theta),$$

$$y \rightarrow \eta = \frac{1}{2} \ln \left(\frac{1 + \beta \cos \theta}{1 - \beta \cos \theta} \right)^{\beta-1} = -\ln \tan \frac{\theta}{2}, \quad (5.12)$$

where η is called the *pseudorapidity*. The R -measure, or cone radius for simple cone jet algorithms, is in terms of η and ϕ , the azimuthal angular separation in the plane transverse to the incoming proton direction, and is given by

$$R = \sqrt{(\eta_1 - \eta_2)^2 + (\phi_1 - \phi_2)^2} \quad (5.13)$$

where the 2π periodicity of ϕ must be explicitly removed by taking ϕ differences in the range $[-\pi, \pi]$.

Over the last two decades, cone and clustering techniques have advanced in sophistication and variety. A number of jet reconstruction algorithms are in common use, including, for example, the iterative cone and variants thereof, midpoint-cone, SIScone (Seedless Infrared Safe Cone), the inclusive k_T , the anti- k_T , and the Cambridge-Aachen jet algorithms. The jet algorithms may be used with different *recombination schemes* for

adding the constituents. In the *energy scheme*, constituents are added as four-vectors, where the final four-vector describing the jet has a finite mass.

To give an explicit example, in the iterative cone algorithm an E_T -ordered list of input objects (particle tracks or calorimeter towers) is created, where E_T is shorthand for the transverse momentum of a massless calorimeter object. A cone of size R in (η, φ) -space is cast around the input object having the largest transverse energy above a specified *seed threshold*. The objects inside the cone are used to calculate a *proto-jet* direction and energy. The computed direction is used to seed a new proto-jet. The procedure is repeated until the energy of the proto-jet changes by less than 1% between iterations and the direction of the proto-jet changes by $\Delta R < 0.01$. When a stable proto-jet is found, all objects in the proto-jet are removed from the list of input objects and the stable proto-jet is added to the list of jets. The whole procedure is repeated until the list contains no more objects with an E_T above the seed threshold. The cone size and the seed threshold are parameters of the algorithm. When the algorithm is terminated, a recombination scheme, such as the energy scheme, is applied to jet constituents to define the jet kinematic properties.

Cone algorithms, such as the midpoint cone, can be designed to facilitate the splitting and merging of jets for a pair of jets closely spaced in R . In the midpoint cone, contrary to the iterative cone algorithm described above, no object is removed from the input list. This can result in overlapping proto-jets (a single input object may belong to several proto-jets). To enhance the *collinear* and *infrared safety* of the algorithm, a second iteration of the list of stable jets is done. For every pair of proto-jets that are closer than the cone diameter, a *midpoint* is calculated as the direction of the combined momentum. These midpoints are then used as additional seeds to find more proto-jets. When all proto-jets are found, the following splitting and merging procedure is applied, starting with the highest E_T proto-jet. If the proto-jet does not share objects with other proto-jets, it is defined as a jet and removed from the proto-jet list. Otherwise, the transverse energy shared with the highest E_T neighbor proto-jet is compared to the total transverse energy of this neighbor proto-jet. If the fraction is greater than f (typically 50%), the proto-jets are merged; otherwise the shared objects are individually assigned to the proto-jet that is closest in (η, φ) -space. The procedure is repeated, again always starting with the highest E_T proto-jet, until no proto-jets are left. This algorithm implements the energy scheme to calculate the proto-jet properties but a different recombination scheme may be used for the final jet. The parameters of the algorithm include a seed threshold, a cone radius, a threshold f on the shared energy fraction for jet merging, and also a maximum number of proto-jets that are used to calculate midpoints.

The inclusive k_T , anti- k_T , and Cambridge-Aachen jet algorithms are cluster-based jet algorithms [4]. The cluster procedure starts with a list of input objects, stable particle tracks, or calorimeter cells. For each object i and each pair (i, j) the following distances are calculated:

$$\begin{aligned} d_{iB} &= (k_{T,i})^{2p}, \\ d_{ij} &= \min\{k_{T,i}^{2p}, k_{T,j}^{2p}\} R_{ij}^2 / R^2 \quad \text{with} \quad R_{ij}^2 = (\eta_i - \eta_j)^2 + (\varphi_i - \varphi_j)^2, \end{aligned} \quad (5.14)$$

where $k_{T,i}$ is the transverse momentum of the i th particle with respect to the beam axis. The parameter R is typically set in the range $R = 0.1$ for extremely narrow jet substructure to

$R = 1.0$ to encompass the bulk of the total particle flow from all particles produced from a jet generated by a quark or gluon. The parameter $p = 1, 0, -1$ is set to a value that corresponds to the inclusive k_T , Cambridge-Aachen, and anti- k_T jet algorithms, respectively. Here $p = 1$ begins clustering with the lowest k_T objects while $p = -1$ begins with the highest k_T objects. The quantity d_{iB} is called the particle-beam distance as it sets a reference for object i for the transverse momentum relative to the beam direction. The clustering algorithm searches for the smallest d_{iB} or d_{ij} . If a value of type d_{ij} is the smallest, the corresponding objects i and j are removed from the list of input objects, merged using one of the recombination schemes and filled into the list as one new object. If a distance of type d_{iB} is smaller or equal to d_{ij} , then the corresponding object i is removed from the list of input objects and filled into the list of final jets. The procedure is repeated until all objects are included in jets.

Once a jet list is formed, it is natural to evaluate the energy resolution of the resulting objects as they relate to the expected four-vector summation for the particles forming the jet, and also at a deeper level to the quark or gluon that initiated the jet. The jet energy resolution at hadron colliders is typically fitted with the following functional form:

$$\frac{\sigma_{E_T}}{E_T} = \frac{N}{E_T} \oplus \frac{S}{\sqrt{E_T}} \oplus C, \quad (5.15)$$

added in quadrature according to equation (5.6) where the first term is due to fixed energy fluctuations in the cone from electronics noise and also, as described in chapter 8, from minbias pile-up, and *underlying-event* energy; the second term comes from the stochastic fluctuations of the hadronic calorimeter measurements; and the last term is the constant term from residual nonuniformities and nonlinearities in the detector response.

The average particle p_T in a jet predicted for LHC 7 TeV-on-7 TeV proton-proton collisions is plotted in figure 5.10 versus jet p_T for $R = 1.0$ iterative cone jets. Similarly, the particle multiplicity in jets for $R = 0.5$ and $R = 1.0$ iterative cone jets is plotted in figure

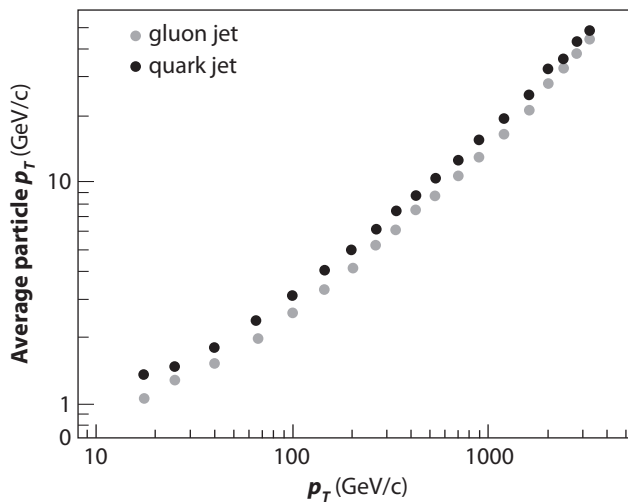


FIGURE 5.10. Average particle p_T in a gluon or light quark jet as a function of jet p_T , as estimated from simulation.

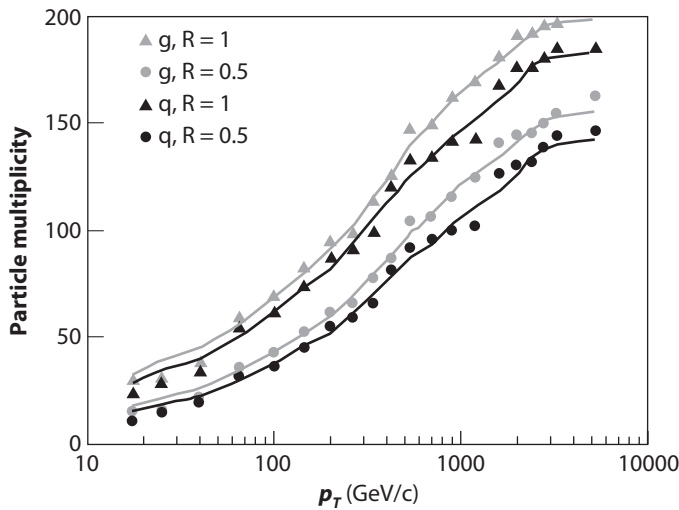


FIGURE 5.11. Average particle multiplicity in gluon (g) and light quark (q) jets within a cone radius of $R = 0.5$ and $R = 1.0$ as a function of jet p_T , as estimated from simulation.

5.11 where the particle content of the jets, in terms of particles impacting the calorimeter, is dominated by charged pions and photons from π^0 decay. Excluding jets with leptons from semileptonic decay, one sees typically $\sim 75\%$ of the visible energy flow in hadrons, about 80% of which are charged hadrons. The remaining $\sim 25\%$ of the visible energy flow is in photons, where there are large jet-to-jet fluctuations on the fraction of π^0 versus π^\pm .

5.6 *b*-Jets and Vertex Detectors

The finite lifetime of *B*-hadrons introduces a unique ability to identify jets originating from *b*-quarks, so-called *heavy flavor* jets. A typical beam pipe radius in a collider experiment is at least 4 cm. A *B*-hadron produced with an energy of 35 GeV after fragmentation will have a decay length of $\sim 2\text{--}3$ mm, well within the beam pipe. Therefore, the tracking detectors must accurately extrapolate charged particle trajectories back into the vacuum region of the beam pipe to determine their point of origin. To accomplish this, a vertex detector is positioned directly outside the beam pipe, where the beam pipe is typically made out of beryllium or other low multiple-scattering materials. A vertex detector must handle a high flux of closely spaced particles coming from jets, multiple interactions, and highly boosted short-lived particles as well as processes such as photon conversion in the beam pipe.

The strategy of using a vertex detector is to provide unambiguous three-dimensional spatial points unique to each charged-particle trajectory and to provide at least three radial layers of measurements to enable a minimal level of track-finding capability. This is achieved with the use of a silicon pixel detector. Pixel sensors are typically $200\text{--}300\ \mu\text{m}$

thick with individual pixel dimensions of 50–100 μm in width in the bending plane and 150–400 μm in length along the beam pipe axis. The total number of individual channels in an LHC pixel detector is nearly 100 megapixels.

Pixel detector coordinates simultaneously improve the accuracy of the track extrapolation back into the collision region and the momentum resolution of the combined tracker, despite the relatively minor increase in measurement lever arm for the track curvature. Several parameters are needed to determine the helicoidal trajectory of a charged particle. A measurement improvement on the distance of closest approach, as determined from a pixel detector, can therefore translate into an improvement in the momentum resolution when the track parameters are heavily correlated. To take into account finite scattering in the tracking material, a *Kalman filter* or *Gaussian-sum filter* is used to propagate nonideal charged-particle trajectories.

One of the most important measurements of the tracking system is the *primary vertex* location. The primary vertex is the spatial location of where two particles in the colliding beams interacted. With a pixel detector, the primary vertex can be determined to better than 10–50 μm in all three spatial coordinates depending on the track momenta and multiplicity. In the case of heavy flavor production there are multiple vertices in the event. The first is a collection of charged tracks produced promptly at the primary vertex from strong-interaction decays. The second set are *secondary vertices* that originate from the *B*-hadron decay, one from each jet, and there is potentially a third set of *tertiary vertices* that come from the finite lifetime of *D* mesons and kaons produced in *B*-hadron decay. Figure 5.12 shows an example of a *b*-tagging in a heavy flavor jet. A typical measure of the sensitivity for detecting secondary vertices is the resolution of the miss distance or *impact parameter* of a track to the primary vertex. The impact parameter resolution typically varies from 10 μm to 100 μm corresponding to 100 GeV/*c* and 1 GeV/*c* track transverse momenta p_T , respectively. A collection of tracks with significant impact parameters and therefore low

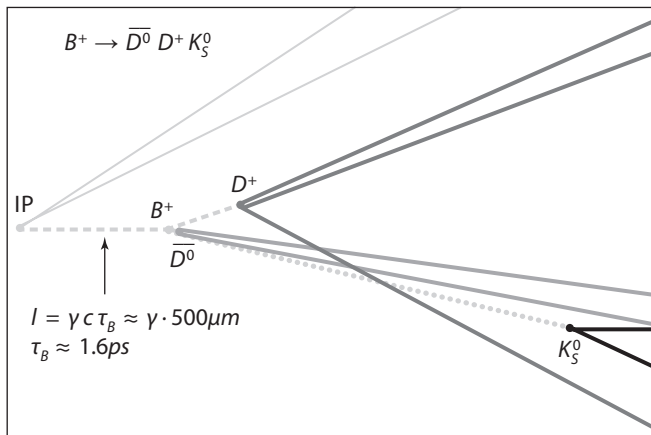


FIGURE 5.12. The figure shows the reconstructed primary vertex, also known as the interaction point (IP), to the left. In the center is the secondary vertex from the *B*-hadron decay. Additional tertiary vertices are found for the *D*-meson and neutral kaon decays (Credit: ALEPH).

probabilities to come from the primary vertex are used to compute the probability that a jet contains a heavy flavor hadron. A jet containing a secondary vertex has a high probability to be a jet originating from an energetic b -quark parton or, with lower sensitivity, a c -quark. There is, however, a finite probability that heavy flavor hadrons are formed in the hadronization stage of jet production, such as in the process of *gluon splitting* to a heavy quark-antiquark pair.

Impact parameters will have a *lifetime sign* indicating whether the decay length from the track is on the side of the jet relative to the primary vertex or whether it is in the *negative lifetime* region. The negative lifetime distribution is a valuable measure of the finite resolution for secondary vertex tagging and the expected mistag rate for measuring a false positive-lifetime secondary vertex. For a 60% lifetime b -tagging efficiency for heavy flavor jets, the typical mistag rate is 1% or less for light quark (excluding charm) and gluon jets. The mistag rate performance curve of the lifetime b -tagging algorithm typically increases exponentially with b -tagging efficiency where it is common to use mistag rates between 0.1% and a few percent depending on the efficiency needed. An alternative method for identifying b -jets is to search for the semileptonic decay of a B -hadron producing a charged lepton, electron or muon, with a large momentum and relatively large transverse momentum with respect to the jet axis owing to the large mass of the B -hadron. The *soft lepton* tagging method, which has 10–15% efficiency for a 1% mistag rate, is often used to estimate the performance of the lifetime tagging algorithm.

5.7 τ -Leptons

The τ -lepton is unique among the leptons in that it can decay into hadrons. Table 5.1 lists the charged-lepton properties and several of the τ -lepton decay modes. A hadronically decaying τ -lepton has properties similar to QCD jets, but with tight restrictions on the invariant mass, angular width, and charge multiplicity. Typically, the decay products are well-contained within a $\Delta R = 0.3$ cone jet, and the charge multiplicity is dominantly one-prong and three-prong with an average visible energy of 80% of the initial τ -lepton energy. The primary hadronic- τ categories are one-prong with no EM depositions in the calorimeter, one-prong with at least one EM shower, and inclusive three-prong final states. Typically, hadronic τ -leptons can be identified with an overall efficiency of 40% with a QCD jet fake rate of 0.1%.

The dominant one-prong and three-prong decays of τ -leptons and the expected visible mass distribution are shown in figures 5.13 and 5.14, respectively, for selected τ -lepton candidates in Tevatron data. The identification of hadronic- τ decays relies on the narrowness and isolation of the τ -jet. Figures 5.15 and 5.16 show the definition and performance, respectively, of a “shrinking cone” method for separating τ -jets from QCD jets. Due to the finite mass of the τ -lepton, a higher p_T boost will result in a narrower jet of particles from its decay.

The leptonic decays appear much the same as single-electron or single-muon production, providing a wide range of visible momenta in the final-state charged lepton.

Table 5.1 Decay modes, branching fractions, and properties of the charged leptons. A summary of τ -lepton branching fractions in 1-, 3- and 5-pronged charged-track final states is listed.

Lepton	Decay modes	Br (%)	Mass (MeV)	Decay Lifetime
e^-	stable		0.511	$> 4 \times 10^{26}$ years
μ^-	$\rightarrow e^- \bar{\nu}_e \nu_\mu$	~ 100	105.7	2.197 μ s
τ^-	$\rightarrow e^- \bar{\nu}_e \nu_\tau$	17.8	1777	0.29 ps
	$\rightarrow \mu^- \bar{\nu}_\mu \nu_\tau$	17.4		
	$\rightarrow \pi^- \nu_\tau$	10.9		
	$\rightarrow \pi^- \pi^0 \nu_\tau$ (including ρ^-)	25.5		
	$\rightarrow \pi^- \pi^0 \pi^0 \nu_\tau$	9.3		
	$\rightarrow \pi^- \pi^0 \pi^0 \pi^0 \nu_\tau$	1.0		
	$\rightarrow \pi^- \pi^+ \pi^- \nu_\tau$	9.0		
	$\rightarrow \pi^- \pi^+ \pi^- \pi^0 \nu_\tau$	2.7		
	$\rightarrow K^- \nu_\tau$	0.7		
	$\rightarrow \bar{K}^0 \pi^- \nu_\tau$	0.9		
	other	4.8		
τ^-	all 1-prong (non-leptonic)	50.1		
	all 3-prong	14.6		
	all 5-prong	0.1		

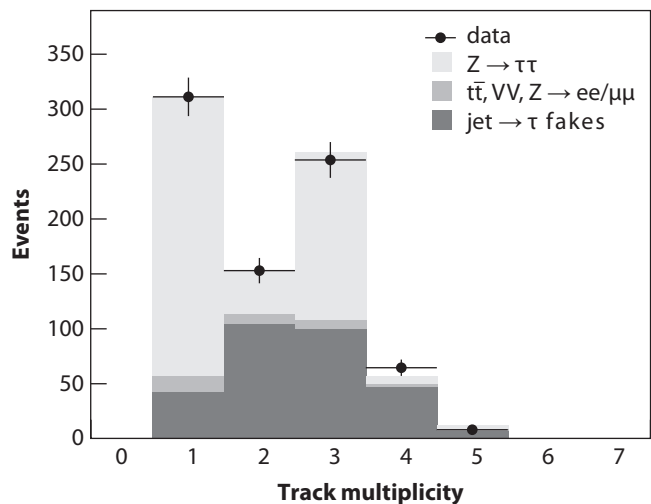


FIGURE 5.13. Track multiplicity in selected τ -lepton candidates before requiring an oppositely charged pair of τ -leptons in the event. Even numbers of tracks indicate track finding inefficiencies in the measurement (Credit: CDF/J. Conway).

However, decays to $\tau^+ \tau^-$ or $\tau^+ \nu_\tau$ can provide constraints for identifying and even partially recovering the missing momentum carried by the τ -neutrinos. The finite lifetime of the τ -lepton provides the possibility that heavily boosted τ -leptons, including those that decay leptonically, can be identified by the finite impact parameters of the charged particles in their decays.

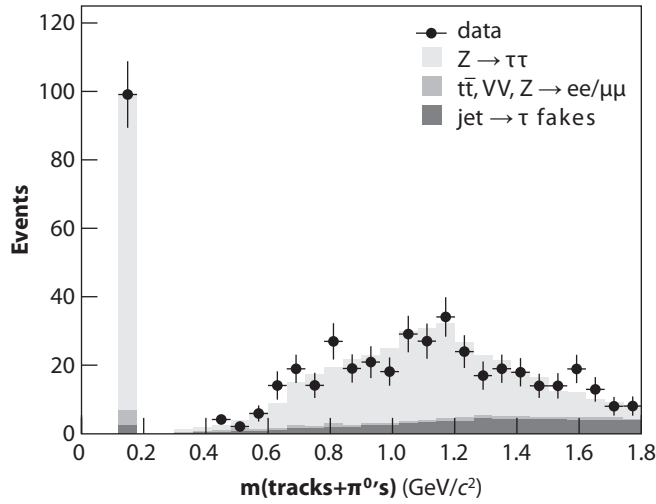


FIGURE 5.14. Reconstructed visible mass of selected τ -lepton candidates. The spike at the pion mass corresponds to one-prong pion decays (Credit: CDF/J. Conway).

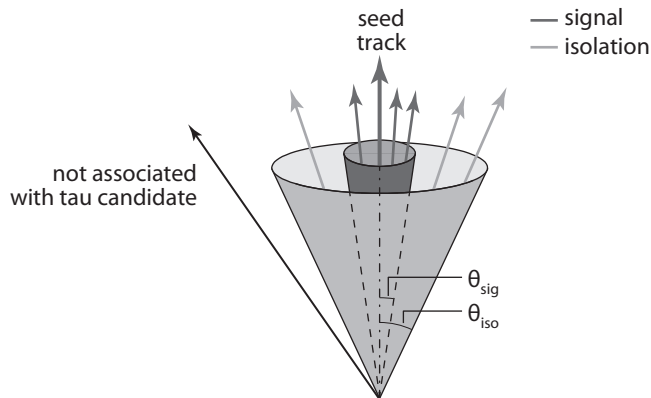


FIGURE 5.15. Cone definitions used for τ -lepton identification with a central signal cone containing the τ -lepton decay products and the outer isolation cone used to veto against QCD jet fakes (Credit: CDF/J. Conway).

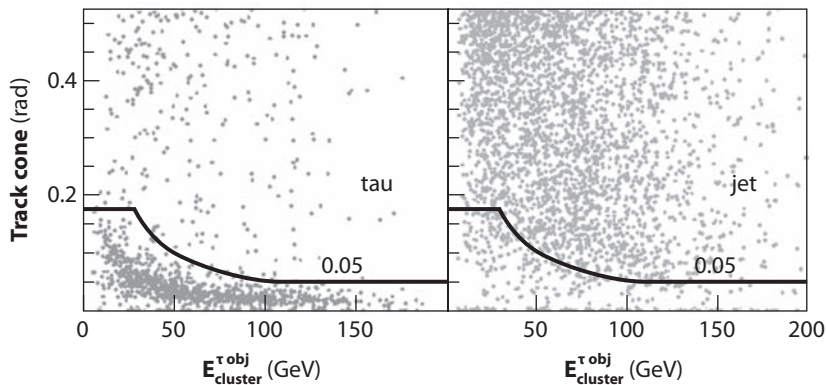


FIGURE 5.16. Jet/ τ -lepton separation showing that a dynamically shrinking signal cone as a function of the visible τ -lepton energy is a powerful discriminator against QCD jet fakes (Credit: CDF/J. Conway).

5.8 Missing Transverse Energy

Beginning with the UA1 experiment at CERN (1981–1993), all major detectors at hadron colliders have been designed to cover as much solid angle as practically possible with calorimetry. The primary motivation of this is to provide as complete a picture as possible of the event, including the presence of one or more energetic neutrinos or other weakly interacting stable particles through apparent missing energy. Energetic particles produced in the direction of the beam pipe make it impossible to directly measure missing energy longitudinal to the beam direction; however, the transverse energy balance can be measured with an accuracy good enough to help establish a physics signature involving one or more noninteracting particles. The W boson was discovered and its mass determined to 3% with just six events due to the ability of UA1 to infer the presence of 40 GeV neutrinos with a resolution of a few GeV. Since the time of the W discovery, measurement of missing transverse energy has been a major tool in the search for new phenomena at hadron colliders.

The missing transverse energy vector is calculated by summing individual calorimeter towers having energy E_n , polar angle θ_n , and azimuthal angle ϕ_n :

$$\vec{E}_T^{\text{miss}} = -\sum (E_n \sin \theta_n \cos \phi_n \hat{\mathbf{i}} + E_n \sin \theta_n \sin \phi_n \hat{\mathbf{j}}) = E_x^{\text{miss}} \hat{\mathbf{i}} + E_y^{\text{miss}} \hat{\mathbf{j}} \quad (5.16)$$

or, alternatively, using pseudorapidity

$$\vec{E}_T^{\text{miss}} = -\sum \left(\frac{E_n \cos \phi_n}{\cosh \eta_n} \hat{\mathbf{i}} + \frac{E_n \sin \phi_n}{\cosh \eta_n} \hat{\mathbf{j}} \right) = E_x^{\text{miss}} \hat{\mathbf{i}} + E_y^{\text{miss}} \hat{\mathbf{j}}. \quad (5.17)$$

Reconstructed muons are taken into account by subtracting the expected minimum ionizing calorimeter deposit (typically 2–3 GeV) and vectorally adding the muon track transverse momentum as measured by the muon spectrometer. When jet energy scale calibrations are applied to the event, the corresponding (type-1) correction to the E_T^{miss} is given by

$$E_{T(x(y))}^{\text{miss}} = - \left[E_{T(x(y))}^{\text{raw}} + \sum_{\text{jets}} (p_{T(x(y))}^{\text{corr, jet}} - p_{T(x(y))}^{\text{raw, jet}}) \right]. \quad (5.18)$$

An alternative to applying type-1 corrections is to calibrate the E_T^{miss} object inputs before running the algorithms, and thus avoid having a jet p_T threshold when it comes to applying energy scale corrections. An advanced method for the calibration of input objects is known as *particle flow*. The particle-flow technique uses a wide range of detector information from the tracking system and calorimeters to identify and extract the energy and momentum of the individual stable particles, hadrons, photons, and leptons, in the event. The collection of particle-flow objects provides a complete picture of the particle types, energies and momenta and, thus, form the basis for all measurements in the high-energy event.

The E_T^{miss} resolution is dependent on the overall activity of the event, characterized by the scalar sum of transverse energy in all calorimeter cells, denoted ΣE_T . The resolution of E_T^{miss} for an intrinsically balanced event can be measured by the width along any fixed spatial direction, i.e., the x - or y -component (E_x^{miss} or E_y^{miss}) of missing transverse energy, as a function of ΣE_T . The resolution for balanced QCD *dijet events*, as arise from $2 \rightarrow 2$

scattering, is observed to be described by the function $\sigma_{E_T^{\text{miss}}} = S' \sqrt{\Sigma E_T}$, E_T in units of GeV, owing to the stochastic effects of calorimeter showers where S' is a parameter related to the calorimeter energy resolution, typically $S' = 40\text{--}100\%$ for calorimeter-based inputs. For particle-flow inputs, on the other hand, the effective stochastic term can be substantially reduced due to the nonstochastic nature of tracking system measurements. In the high-scalar-sum E_T region, eventually the constant term, typically 1–2% added in quadrature according to equation (5.6), will dominate the E_T^{miss} resolution. For nonzero E_T^{miss} , as in the case of neutrinos from W-boson decay, Z bosons decaying to neutrinos, and the possibility of heavy weakly interacting particles produced in collisions, it is common to estimate the significance of a nonzero E_T^{miss} with the E_T^{miss} significance given by

$$\text{Sig}(E_T^{\text{miss}}) \propto \frac{|E_T^{\text{miss}}|}{\sqrt{\Sigma E_T}} \quad (5.19)$$

where a large significance is more likely to originate from a weakly interacting particle than from mismeasurement in an intrinsically p_T -balanced process. A more detailed evaluation of the E_T^{miss} significance involves the angles of the E_T^{miss} and the measured objects, where the angular measurements are generally more precise than the energy measurements and, therefore, the significance is enhanced if the measured E_T^{miss} points in a direction inconsistent with the energy measurement uncertainties alone.

It is also common practice to form event variables that describe the total scalar sum p_T and the missing transverse momentum p_T^{miss} that are constructed directly from high- p_T objects, such as jets, leptons, and photons. The variable, H_T , is the scalar sum of the jet p_T for all jets with a jet $p_T > p_{T,\text{min}}$, where $p_{T,\text{min}}$ is the minimum jet p_T threshold, typically 10–30 GeV. As jets have a finite jet mass, it is important to consider the p_T of the jet, rather than simply the E_T as is used for calorimeter cells. Similarly, one can define MH_T as the missing transverse momentum vector computed from the negative of the vector sum of the jet p_T vectors, for jets above a minimum jet p_T threshold. The properties of these quantities are similar to ΣE_T and E_T^{miss} but are less sensitive to electronic noise in the calorimeters and low- p_T isolated hadrons.

5.9 Neutrinos and Water Cherenkov Detectors

The water Cherenkov detector is a novel detector geometry consisting of a large volume of water or mineral oil viewed from all directions with UV-sensitive photomultiplier tubes (PMTs). The first large-scale experiments utilizing this concept, the IMB and Kamioka experiments, were originally designed to detect the $SU(5)$ GUT prediction of proton decay via lepto-quark interactions in the mode $p \rightarrow e^+ \pi^0$. The energetic EM shower from the positron emitted in the hypothetical proton decay would generate Cherenkov radiation with a conical opening angle along the three-momentum direction of the positron. A similar set of radiation cones are generated from the photons of the π^0 decay. One of the primary backgrounds in the proton decay experiments comes from cosmic muons and *spallation* products of nearby interactions. A relativistic muon passing through the water

volume will produce a similar Cherenkov cone, better defined in angle due to the reduced angular scattering of muons passing through water relative to that of electrons, with a high brightness due to the large path length and with a distribution of momentum directions characteristic of the muon source, where cosmic muons are dominantly downward going. The patterns of Cherenkov light from different sources are detected with a large array of PMTs pointing inward to the center of the water volume from all directions. Example patterns are shown in figure 5.17.

The large volume and powerful particle identification capabilities of water Cherenkov detectors are particularly well-suited for neutrino experiments, and, indeed, the IMB and Kamioka experiments were the first to detect a neutrino burst from a supernova. Large-volume water Cherenkov detectors, such as the 30,000 tons of water in the Super-Kamiokande detector, are capable of measuring signals from interactions induced by neutrinos originating from a wide range of sources including weak processes in the Sun,

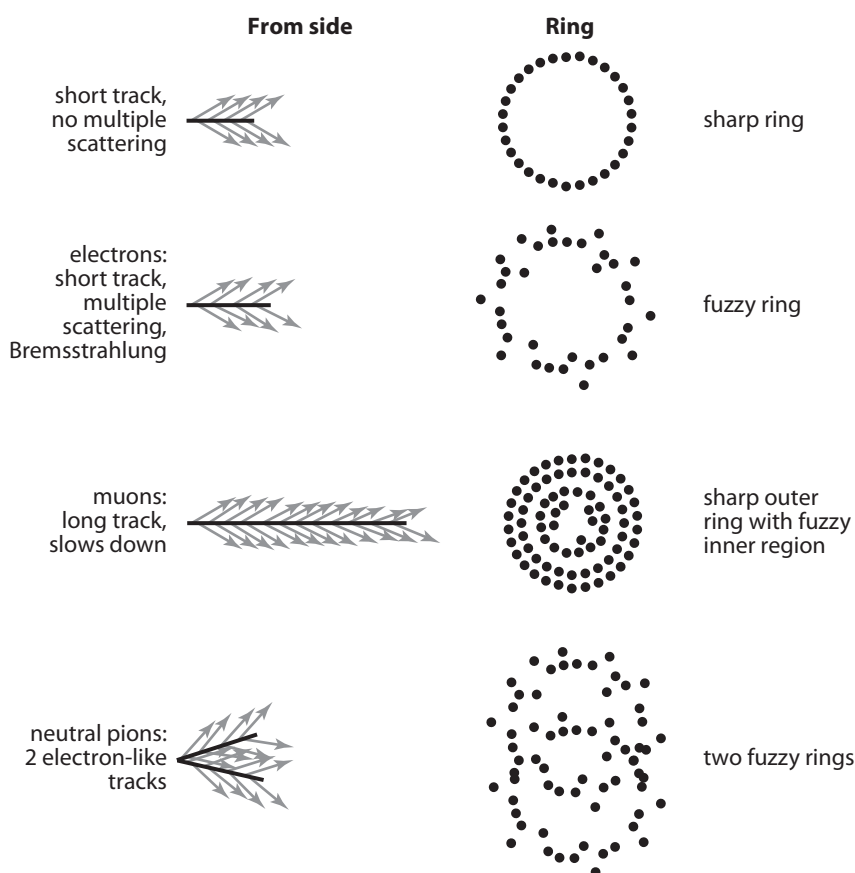


FIGURE 5.17. Cherenkov radiation patterns from different particles traveling through water or mineral oil at relativistic velocities. The patterns are measured by spatial arrays of photomultiplier tubes that point inward toward the center of the volume of liquid from all directions (Credit: BOONE/J. Conrad)

neutrinos produced from cosmic rays in Earth's atmosphere, and accelerator-based neutrino sources.

5.10 Dark Matter Detectors

Not all the matter in the universe is accounted for in the Standard Model of particle physics. Nearly one-quarter of the mass in the universe is attributed to nonbaryonic cold *dark matter*. The low level of self-interaction of the cold dark matter is consistent with a particle physics model for direct detection known as Weakly Interacting Massive Particles (WIMPs). WIMP particles are predicted to fill all of space in the form of an extremely low density, electrically neutral gas having particle number densities of approximately $10^3/\text{m}^3$ with a particle mass in the range 40–1000 GeV/c^2 .

One technique for WIMP detection is to look for anomalous nuclear recoils in a low-background Earth-based detector. The kinetic energy of the WIMPs is set by the velocity at which Earth travels through the *galactic halo*, yielding kinetic energies of order 10 keV for WIMPs in the rest frame of an Earth-based detector and introducing a directionality in the scattering process. Low-temperature, typically 20 mK, solid-state germanium and silicon detectors such as those used in the CDMS and Edelweiss experiments can measure keV-scale energy depositions to high precision. The low thermal capacity of solids at low temperature enables these detectors to be sensitive to *phonons* from nuclear recoil, quanta of heat dissipation that propagate as sound waves in the detector. Cryogenic solid-state detectors can isolate the very low-ionization nuclear recoils expected in WIMP interactions from background processes with larger ionization signals typical of β -decay and gamma-ray sources from radiative contaminants and cosmic-muon induced spallation backgrounds. Neutron and spallation backgrounds are reduced substantially by locating these detectors deep underground. Neutrons can be further separated from WIMPs by their tendency to scatter multiple times in the detector volume.

Cryogenic noble liquids are also effective dark matter detectors. Although the energy deposition from ionization has lower calorimetric energy resolution than solid-state detectors, the ionization electrons can be drifted out of the noble liquid into a gaseous region where single-electron gas-gain amplification can be used to enhance the detection sensitivity to ionization signals. The lower density of noble gas liquids relative to germanium can be compensated by larger detector volumes employing geometries similar to the water Cherenkov detectors described above. The location of the nuclear recoil within the active detector volume can be determined using the coordinate of the drifted ionization and the drift time relative to an associated light scintillation signal produced in the noble liquid and detected with a dense spatial array of photodetectors facing the active liquid volume. The light scintillation signals generated in the noble liquid from nuclear recoil act in much the same sense as the phonon signals in solid-state detectors. The ratio of the ionization to scintillation is much lower for nuclear recoils than for β -decay or gamma-ray sources. The pulse shape and timing of the scintillation relative to the ionization is also an effective discriminator to identify the time-delayed nuclear recoil scintillation signal.

The push for large-volume, low-background dark matter detectors located deep underground is a rapidly expanding field of particle physics.

5.11 Exercises

1. A photon of energy 10 GeV interacts with the material of the beam pipe to pair produce into an electron and positron, each with $p_T = 5$ GeV/c. Compare the expected electromagnetic calorimeter energy resolution for a 10 GeV photon with $N = 0.1$ GeV, $S = 5\%$, and $C = 0.05\%$ with a tracker measurement of the total p_T of the electron-positron tracks from the converted photon. For the tracking system, use $c_0 = 1.5\%$ and $c_1 = 2 \times 10^{-4}$ (GeV/c) $^{-1}$. For what photon energy is the energy resolution of the calorimeter equal to that of the converted photon using the tracking system to measure the p_T ?
2. For some measurements, the electron energy measurement is made with the electromagnetic calorimeter, and the tracking system is primarily used to determine the sign of the electron, i.e., whether it is an electron or positron. For high- p_T tracks there will be a finite probability for *charge confusion*, namely, the mismeasurement of the charge q . This is most clearly seen plotting the q/p_T distribution which is proportional to the sagitta of the tracks. If $\sigma_{p_T}/p_T = 100\%$ for a given track p_T , what is the average charge confusion at this value of p_T ? Recall that 68% of a Gaussian distribution is within one standard deviation of the mean. The rate of charge confusion is typically lower for a muon spectrometer at high p_T relative to an inner tracking system. Describe an algorithm for using the muon chambers with a finite but lower charge confusion rate to determine the charge confusion rate of the inner tracker for a given sample of muons having a range of measured p_T values.
3. Compute the ratio of the charged pion-to-electron response, π/e , for a pion shower with a π^0 fraction, $f_{\pi^0} = 0.7$, and a noncompensating calorimeter with an e/h value of $e/h = 1.4$.
4. Compute the number of Gaussian sigma separation between the reconstructed mass peaks of a W boson and a Z boson decaying at rest to a pair of jets. Assume the calorimeter has a jet energy resolution with $N = 1$ GeV, $S = 30\%$, $C = 4\%$, and a negligible angular resolution. Repeat the same calculation for $S = 50\%$.
5. A particle with a mass of 115 GeV decays to a pair of b -jets. If the particle is produced with $p_T = 350$ GeV and decays into a pair of jets, what is the ΔR separation of the jets for equal energy jets in the lab frame? Suppose the jet reconstruction is run with a large jet cone size of $R = 1.5$. How could one reconstruct a mass peak of the 115 GeV particle using large jets?
6. Assume the Z boson is produced at rest and decays to a pair of τ -leptons. If the τ^- decays to $\rho^- \nu_\tau$ with the ρ^- carrying 80% of the initial τ -lepton energy, estimate the

separation of the π^- and π^0 from the ρ decay in the lab frame assuming the π^- and π^0 share equally the initial ρ^- energy. Repeat the analysis for the photon separation in the lab frame for the subsequent $\pi^0 \rightarrow \gamma\gamma$ decay assuming equal energy photons.

7. A 1 TeV/c muon is produced and measured with an inner tracking system with parameters $c_0 = 1.5\%$ and $c_1 = 2 \times 10^{-4} \text{ (GeV/c)}^{-1}$. The muon spectrometer also measures the same muon with a combined tracking system p_T resolution of $c_0 = 3.0\%$ and $c_1 = 10^{-4} \text{ (GeV/c)}^{-1}$. What is the muon momentum resolution for a 1 TeV/c muon for the inner tracking system alone and for the combined inner plus muon spectrometer tracking system?
8. A J/Ψ resonance with a mass of approximately $3.1 \text{ GeV}/c^2$ is produced with an energy of 30 GeV in the lab frame and decays to a pair of electrons. For equal electron energies and an electromagnetic calorimeter with a radius of 1.2 m and a Molière radius of 2 cm, will the two electromagnetic showers be distinguished? Consider the two tracks from the J/Ψ at a radius of 4 cm at the location of the first layer of pixel detectors. What is the maximum spatial separation of the charged tracks, neglecting magnetic field, and how does it compare with a pixel spacing of $50 \mu\text{m}$?
9. **Soft-pion tagging of charm production.** The mass difference of the $D^{*\pm}$ meson and the D^0 meson is 145.4 MeV and the D^0 meson has a 3.8% branching ratio to $K^-\pi^+$. Describe the experimental signature that could be used to identify charm production using the tracking system.
 - (a) In the rest frame of the D^0 meson, what is the magnitude of the momentum of the K^- from the $K^-\pi^+$ two-body decay? Assume that the decay angle of the two-body decay in the rest frame is orthogonal to momentum direction of the D^0 in the lab frame. If the momentum of the D^0 meson in the lab frame is $p = 3 \text{ GeV}/c$, what are the magnitudes of the K^- and π^+ momenta in the lab frame?
 - (b) What is the magnitude of the momentum of the soft pion from $D^{*\pm}$ decay in the lab frame, assuming the pion is produced at rest in the $D^{*\pm}$ rest frame and the D^0 meson has a momentum of $p = 3 \text{ GeV}/c$ in the lab frame?
 - (c) The time-of-flight system is used to distinguish the decay of the D^0 to the $K^-\pi^+$ final state as opposed to the doubly Cabibbo suppressed decay $K^+\pi^-$. What is the required timing resolution (Gaussian standard deviation) of the time-of-flight system required to get three standard deviations of separation of kaons and pions over a flight distance of $L = 2 \text{ m}$ for a D^0 -meson decay as described in part (a)?
10. The cross section for a charged kaon to interact with a proton is typically 20% lower than for a charged pion to interact with a proton. If the fraction of charged pions that punch through the hadron calorimeter is 10^{-4} , what is the corresponding fraction for charged kaons assuming the same momentum spectrum?
11. The cross section for a 1 GeV/c K^- to interact with a proton or neutron is over a factor of 2 larger than that for a K^+ . This phenomenon leads to more K^+ mesons

punching through the calorimeter and therefore an excess of positively charged muon candidates detected by the muon spectrometers. What final states are available to $K^- + N$ scattering interactions, where N is a nucleon, that have no analogue for $K^+ + N$ scattering?

12. The ratio of the hadronic calorimeter energy response for 2 GeV π^+ compared to π^- is found to be 110% on average in a noncompensating calorimeter. What subset of interactions is causing this asymmetry? Assume the calorimeter is made of material with heavy nuclei.
13. The number of interactions per bunch crossing of a proton-proton collider at high luminosity can be 20 events or more. Assuming these are *minimum bias* events which typically have $\sum E_T = 35$ GeV each, what is the nominal E_x^{miss} resolution for $S' = 45\%$ and a constant term, $C' = 2\%$. If, in addition to the 20 minimum bias events, a W boson is produced at rest and decays leptonically, what is the number of sigma separation of the E_T^{miss} from zero?
14. Assume a muon stops in the center of an $R = 10$ m water Cherenkov detector. If the electron from muon decay carries away $m_\mu c^2/2$ of energy, over what path length will the electron Cherenkov radiate? The $dE/dx \approx 2$ MeV/cm for MeV-scale electrons in water and the index of refraction in water is $n = 1.33$. Repeat the same calculation for muons with 500 MeV/c of kinetic energy. The $dE/dx \approx 1.5$ MeV/cm for muons in water with 100 MeV to 1 GeV of kinetic energy.
15. Assume 3 eV is required to produce an electron-hole pair in a solid-state germanium detector at low temperature. Estimate the Gaussian energy resolution on the measurement of a 4 keV X-ray based on electron-hole pair counting statistics alone. Repeat the same calculation for an NaI(Tl) scintillating crystal detector that yields 38 photons per keV.
16. **Cold dark matter.** Our Milky Way has a nearly spherical halo of dark matter that comprises most of its mass. The dark matter is thought to consist of stable, neutral elementary particles. If the particles interact only gravitationally, then simulations suggest that their density should rise sharply as one approaches the galactic center. However, astronomical observations suggest that this is not the case. The dark matter density is nearly constant (about $0.4 \text{ GeV}/c^2/\text{cm}^3$) inside a radius of 2×10^{20} m, about the distance of the sun from the galactic center. Within this radius, particles travel at speeds of about 300 km/s.

The proposed explanation is that the dark matter particles may scatter elastically off one another. The scattering ensures that they cannot pile up in the center of the galaxy and they are more evenly distributed within the galactic core. A few interactions per particle over the lifetime of the universe (15 billion years) suffices to alter their distribution.

- (a) If the dark matter has mass m , estimate the lower bound on the elastic scattering cross section required to alter their distribution.

- (b) Compare the scattering cross section of part (a) to an estimate of the scattering cross section for WIMPs, hypothetical weakly interacting particles with $m \approx 100 \text{ GeV}/c^2$. For example, one could consider WIMPs to have the same quantum numbers as left-handed neutrinos and that the elastic scattering proceeds through the neutral electroweak current.

Suppose the dark matter particles scatter elastically from baryons with the same cross section with which they scatter from themselves. Then, existing dark matter detectors on the surface of Earth or deep underground could, in principle, detect them. However, the particles would first have to penetrate the atmosphere. Assume that the atmosphere consists mostly of nitrogen.

- (c) Using the lower bound for the cross section found in part (a) and assuming $m = 100 \text{ GeV}/c^2$, estimate the interaction length (mean free path) in meters due to scattering in the atmosphere.
- (d) If the particle scatters from a nucleus in the detector, the recoil energy can be detected provided it exceeds 10 eV. Estimate the energy of the particle when it reaches a detector at sea level. Will the particle be detected?

5.12 References and Further Reading

A selection of reference texts and review articles in experimental particle physics can be found here: [5, 6, 7, 8, 9, 10, 11, 12, 13, 14, 15, 16].

A selection of introductory texts on nuclear physics and related methods can be found here: [17, 18, 19].

A selection of Web sites of related experiments can be found here: [20, 21, 22, 23, 24, 25].

A useful tool for looking at experimental data can be found here: [26]. A simulation tool for tracking particles through different detector materials and geometries is found here: [27].

[1] K. Nakamura et al. (Particle Data Group). *J. Phys. G* **37** (2010). <http://pdg.lbl.gov>.

[2] I. Tamm. *J. Phys. U.S.S.R.* **1** (1939) 439.

[3] CMS Experiment Public Results. <https://twiki.cern.ch/twiki/bin/view/CMSPublic/PhysicsResults>.

[4] Matteo Cacciari, Gavin P. Salam, and Greg Soyez. *J. High Energy Phys.*, **04:063** (2008). doi: 10.1088/1126-6708/2008/04/063.

[5] Dan Green, editor. *At the Leading Edge*. World Scientific Publishing, 2010. ISBN 978-981-4304-67-2.

[6] Claus Grupen and Boris Shwartz. *Particle Detectors*. Cambridge University Press, 2008. ISBN 978-0-521-84006-4.

- [7] Dan Green. *The Physics of Particle Detectors*. Cambridge University Press, 2000. ISBN 0-521-66226-5.
- [8] Glenn F. Knoll. *Radiation Detection and Measurement*. Wiley, 2000. ISBN 978-0-471-07338-3.
- [9] Richard Wigmans. *Calorimetry*. Oxford University Press, 2000. ISBN 0-19-850296-6.
- [10] Konrad Kleinknecht. *Detectors for Particle Radiation*. Cambridge University Press, 1998. ISBN 0-521-64854-8.
- [11] R. A. Dunlap. *Experimental Physics*. Oxford University Press, 1988. ISBN 0-19-504949-7.
- [12] Veljko Radeka. *Ann. Rev. Nucl. Particle Sci.* **38** (1988) 217–277. doi:10.1146/annurev.ns.38.120188.001245.
- [13] Thomas Ferbel, editor. *Experimental Techniques in High Energy Physics*. Addison-Wesley, 1987. ISBN 0-201-11487-9.
- [14] William R. Leo. *Techniques for Nuclear and Particle Physics Experiments*. Springer-Verlag, 1987. ISBN 0-387-17386-2.
- [15] Richard C. Fernow. *Introduction to Experimental Particle Physics*. Cambridge University Press, 1986. ISBN 0-521-30170-X.
- [16] Bruno Rossi. *High-Energy Particles*. Prentice-Hall, 1952. ISBN 978-0133873245.
- [17] N. A. Jelley. *Fundamentals of Nuclear Physics*. Cambridge University Press, 1990. ISBN 0-521-26994-6.
- [18] Kenneth Krane. *Introductory Nuclear Physics*. Wiley, 1988. ISBN 0-471-80553-X.
- [19] Emilio Segrè. *Nuclei and Particles*. W. A. Benjamin Publishers, 1977. ISBN 0-8053-8601-7.
- [20] The IMB Experiment (1979–1989). <http://www-personal.umich.edu/~jcv/imb/imb.html>.
- [21] Kamiokande Experiment (1982–1990). <http://www-sk.icrr.u-tokyo.ac.jp/kam/index.html>.
- [22] CDMS-II Experiment. <http://cdms.berkeley.edu>.
- [23] Edelweiss-II Experiment. <http://edelweiss.in2p3.fr>.
- [24] WARP Experiment. <http://warp.lngs.infn.it>.
- [25] XENON Experiment. <http://xenon.astro.columbia.edu>.
- [26] ROOT Analysis Tool. <http://root.cern.ch>.
- [27] GEANT Simulation Package. <http://geant4.cern.ch>.